High-speed force mapping on living cells with a small cantilever atomic force microscope

Christoph Braunsmann, Jan Seifert, Johannes Rheinlaender, and Tilman E. Schäffer[a)]
Institute of Applied Physics and LISA+, University of Tübingen, Auf der Morgenstelle 10, 72076 Tübingen, Germany

(Received 6 May 2014; accepted 16 June 2014; published online 10 July 2014)

The imaging speed of the wide-spread force mapping mode for quantitative mechanical measurements on soft samples in liquid with the atomic force microscope (AFM) is limited by the bandwidth of the z-scanner and viscous drag forces on the cantilever. Here, we applied high-speed, large scan-range atomic force microscopy and small cantilevers to increase the speed of force mapping by ≈10−100 times. This allowed resolving dynamic processes on living mouse embryonic fibroblasts. Cytoskeleton reorganization during cell locomotion, growth of individual cytoskeleton fibers, cell blebbing, and the formation of endocytic pits in the cell membrane were observed. Increasing the force curve rate from 2 to 300 Hz increased the measured apparent Young's modulus of the cells by about 10 times, which facilitated force mapping measurements at high speed. © *2014 AIP Publishing LLC*. [http://dx.doi.org/10.1063/1.4885464]

I. INTRODUCTION

The force mapping imaging mode[1–3] of the atomic force microscope (AFM) can generate maps of the topography and Young's modulus of living cells and thus allows studying their mechanics.[4–8] In the force mapping mode, individual force vs. distance curves ("force curves") are recorded on different xy-positions on the sample surface. A subsequent analysis then reveals the sample topography and the local Young's modulus. The absence of lateral forces on the sample makes force mapping particularly suited for gentle imaging of living cells.[4]

The slow imaging speed of the force mapping mode in a liquid environment, however, hampers the investigations of highly dynamic systems such as living cells. The speed limitation is mainly caused by two components: (i) the z-scanner and (ii) the cantilever.

(i) The z-scanner drives the sample toward the cantilever until the measured force on the cantilever tip exceeds a preselected trigger force, at which point the sample is retracted. The z-scanner may overshoot, owing to inertial effects, resulting in a tip-sample force that exceeds the trigger force. To reduce the overshoot to an acceptable (non-invasive) level, the force curve rate is usually limited to ≈1%–10% of the first resonant frequency of the z-scanner, giving a maximum force curve rate of 10−100 Hz for conventional AFMs.

(ii) The cantilever experiences velocity-dependent viscous drag forces, which introduce measurement artifacts and may lead to sample damage.[4,9–11] Force curve velocities of ≈1−20 μm/s are commonly used on living eukaryotic cells, which limits the force curve rate to ≈0.5−10 Hz.[8,12,13] Larger force curve velocities of up to ≈100 μm/s are possible using the quantitative imaging (QI) force mapping mode by JPK, which uses a "dynamic baseline correction" to correct the viscous drag in the force curves.[14,15]

The overshoot of the z-scanner can be avoided by driving the z-scanner with a sinusoidal voltage and using a feedback loop to keep the maximum tip-sample force constant. This method is used in pulsed force mode[16] and also in PeakForce tapping mode.[17] Force curve rates in the kilohertz-range can be reached in these imaging modes, especially on hard samples in air, which is an enormous speed improvement compared to conventional force mapping. Consequently, especially PeakForce tapping has become popular for mapping mechanical properties over the last few years.[18] However, the speed limitation due to viscous drag forces in liquid remains and becomes particularly relevant when imaging soft samples such as eukaryotic cells that have a Young's modulus of ≈10 kPa or less. The force curve rate in PeakForce tapping is thus typically reduced to ≈250 Hz using a z-range of ≈400 nm when imaging eukaryotic cells in liquid.[19] A larger z-range and thus smaller force curve rate is necessary in the case of very soft, sticky, or highly structured cells to ensure that the tip lifts off the surface in between the force curves. Additionally, the peak force exerted on the sample significantly deviates from the preselected setpoint whenever the sample height or stiffness varies largely between two successive pixels. The distance between two successive pixels must therefore be chosen small enough to ensure a proper tracking of the surface and a gentle imaging. In the force mapping mode, there is no such limitation and the number of force curves per force map can be easily reduced for improving the temporal resolution and for minimizing the overall energy dissipated into the cell.

The speed limitation of the force mapping mode can be overcome by using high-speed atomic force microscopy with small cantilevers.[20–23] The resonant frequencies of high-speed AFM scanners are up to 100 times higher compared to conventional AFM scanners and the viscous drag is significantly

a)E-mail: Tilman.Schaeffer@uni-tuebingen.de. Tel.: +49 7071 29-76030. Fax: +49 7071 29-5093.

reduced when using small cantilevers,[20] which enables much faster force measurements in liquids.[24]

To investigate adherent eukaryotic cells (size usually in between 10 and 100 μm in *xy*-direction and 2–10 μm in *z*-direction) an AFM scanner with a sufficiently large scan range is needed. Achieving large scan ranges and high resonant frequencies at the same time is difficult, since large scanners usually have small resonant frequencies.[25] High-speed atomic force microscopy has thus only rarely been applied to living eukaryotic cells so far.[26–28]

Here, we use an improved version of a high-speed AFM described previously.[23] In combination with small cantilevers, we recorded sequences of high-speed force maps on living mouse embryonic fibroblasts (MEFs) with a resolution of 128 × 128 pixels in less than 1.5 min per map. This is 10−100 times faster compared to conventional force mapping, which allowed us to resolve dynamics of the cytoskeleton and the membrane.

II. EXPERIMENTAL METHODS

A. High-speed atomic force microscope setup

The scanner was an improved version of our previous high-speed, large-range scanner.[23] Piezo stacks in combination with a high-bandwidth piezo amplifier allowed a scan range of 19 μm × 19 μm in *xy* and a *z*-range of 5.5 μm. All piezos were equipped with strain gauge displacement sensors. A strain gauge amplifier (Piezomechanik, Munich, Germany) measured the piezo displacements and provided a noise-level of 21 pm/$\sqrt{\text{Hz}}$ for the *xy*-sensors and 10 pm/$\sqrt{\text{Hz}}$ for the *z*-sensor. Low-pass filtering with a −3 dB cut-off frequency of 3 kHz for the *xy*-sensors and 100 kHz for the *z*-sensor resulted in an RMS noise of 1.2 nm and 2.9 nm, respectively. A self-built analogue feedback controller allowed closed-loop operation in *xy*. The *xy*-scanner's nonlinearity was evaluated by imaging a calibration grid with a pitch of 500 nm, giving <±0.5% over the whole scan range. This is significantly less compared to the nonlinearity when imaging the same area without position feedback (±7%).

A homebuilt optical-lever-based AFM measurement head was used. Its optics produced a diffraction-limited focused spot size of 2.6 μm × 7.2 μm (1/e^2-diameter of the irradiance), which was small enough for the cantilevers used in this study. The cantilevers had an optical transmittance of ≈50%, causing a large fraction of the incident beam to scatter from the sample surface, giving rise to interference fringes in force curves. Using a superluminescent diode (wavelength $\lambda = 680$ nm, power $P = 5$ mW) with a ≈10 times smaller coherence length compared to the conventionally used single mode laser diodes reduced these fringes to an acceptably small level (<0.1 nm). Although the optical interferences are usually unwanted, they also provide an internal ruler for calibrating the *z*-sensor.[29] Using this simple method, the strain gauge *z*-sensor was calibrated and its nonlinearity was found to be <±1% over the full *z*-range.

The high-speed AFM was combined with an optical top view zoom microscope to facilitate the alignment of the focused spot on the cantilever and the coarse positioning of the cantilever relative to the sample (see Fig. 1S in the supplementary material[30]).

To investigate living mammalian cells at 37 °C, we glued a small heatable sample stage on top of the *z*-piezo. This lightweight sample stage (<0.4 g) had a cylindrical shape with a height of 1 mm and a diameter of 6.5 mm. It consisted of a small neodymium magnet, which was wrapped by a heating wire and embedded in a thermally conducting epoxy. A small PT100 resistor was attached to the sample stage to measure its temperature. The thermal expansion of the sample stage in the *z*-direction was only ≈110 nm/°C. The thermal drift could be kept below ±10 nm using a temperature feedback controller.

B. Small cantilevers

Small cantilever prototypes (NanoWorld, Neuchâtel, Switzerland) made of polysilicon [Fig. 1(c)] or silicon nitride (Figs. 1(a) and 1(b), and 1(e), and Figs. 2–7) were used. Both cantilever types had a thickness of 100 nm and a gold reflection coating of 40 nm. The polysilicon cantilevers had a width of 4 μm and a length of 10 μm. The silicon nitride cantilevers were 4 μm wide and 14 μm long. The cantilever tips were formed by electron beam deposition. Their length was 2.5 μm, which was usually large enough to overcome the large height differences of the cells. The tilt of the tips was 10° to compensate for the mounting angle of the cantilever holder [Fig. 1(a)]. The tips had a high aspect ratio with a half-cone angle of only 8° and a nominal tip-end radius of <10 nm [Fig. 1(b)]. The spring constants of the cantilevers were 0.10−0.12 N/m and were calibrated before the measurements by the thermal noise method.[31–33]

Due to thermal drift, the position of the focused spot on the cantilever may change over time. While this drift may be negligible for large cantilevers, it can significantly change the deflection sensitivity of the optical lever sensor for small cantilevers. To account for such changes, we occasionally re-calibrated the sensitivity by the inverse thermal noise method.[34]

C. High-speed force mapping

The local Young's modulus was evaluated by performing a least square fit of Sneddon's contact model for conical tips,[3,35]

$$F = kd = \frac{E}{1-\nu^2}\frac{2\tan\alpha}{\pi}\delta^2, \tag{1}$$

to the approach part of the force curves. Here, F is the force, k is the cantilever spring constant, E is the Young's modulus, and α is the half-cone angle of the tip. An incompressible sample with a Poisson's ratio of $\nu = 0.5$ was assumed. The indentation δ of the tip into the sample was determined from the recorded cantilever deflection d and the *z*-scanner displacement as $\delta = (z - z_0) - (d - d_0)$. Here, z_0 and d_0 are the z-position and cantilever deflection, respectively, when the tip first contacts the sample. To accurately determine the sample indentation, it was necessary to measure the *z*-displacement by a sensor to account for piezo nonlinearity, creep, and hysteresis. We found that the Young's modulus obtained

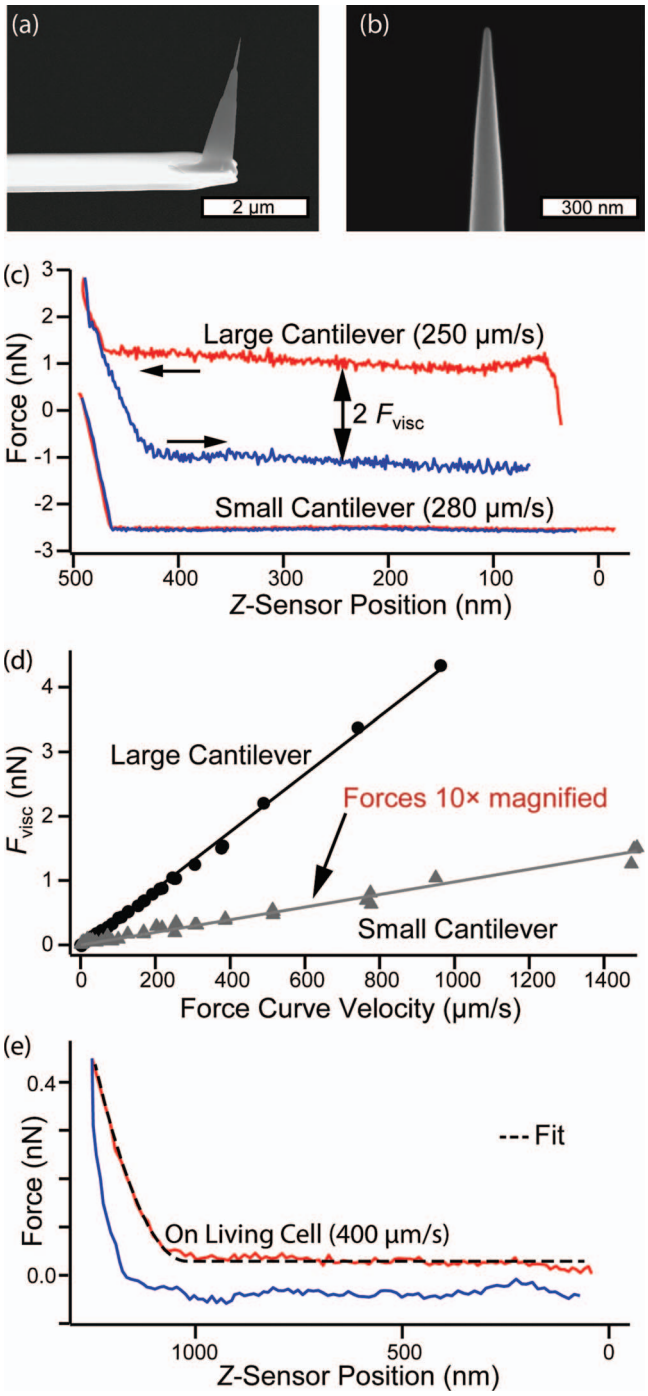

FIG. 1. Small vs. large cantilevers. (a) Side view and (b) close-up of the tip of a small cantilever by scanning electron microscopy. (c) Approach (red) and retract (blue) force curves recorded in distilled water on mica with a large cantilever (upper curve, PNP cantilever, NanoWorld, Neuchâtel, triangular shape, length 200 μm, width 2 × 28 μm, k = 0.053 N/m, first resonant frequency in water at 3.8 kHz) and a small cantilever (lower curve, prototype cantilever, NanoWorld, Neuchâtel, rectangular shape, length 10 μm, width 4 μm, k = 0.12 N/m, first resonant frequency in water at 220 kHz). Both curves were recorded with almost the same force curve velocity (250 μm/s and 280 μm/s, respectively). The curves were vertically and horizontally offset for better visibility. (d) Viscous drag force on the large (black circles) and small (grey triangles) cantilever plotted versus the force curve velocity. A linear function was fitted to the data (straight lines). The forces for the small cantilever were scaled up by a factor of 10 for a better visibility. The viscous drag coefficient (slope of the linear function) was 44 times smaller for the small cantilever than for the large cantilever. (e) Typical force curve recorded with a small cantilever on a living MEF (force curve velocity 400 μm/s).

without the sensor (just by using the piezo drive voltage as it is common practice) deviated by up to a factor of 2 from that when using the sensor.[36] It should be kept in mind that Sneddon's contact model assumes a homogeneous, isotropic, smooth, and linear elastic sample. In reality, cells are highly heterogeneous and textured materials that show nonlinear and viscoelastic behavior. We therefore prefer to term the calculated Young's modulus as "apparent" Young's modulus in the following.

The fit parameter z_0, representing the "contact height", allowed creating an image of the surface topography from the force map data. The "trigger height" z_{trig}, defined as the z-scanner displacement at which the trigger force was reached, gave a topography image of the deformed sample. The apparent Young's modulus E usually varied over several orders of magnitude across the mapped surface and was thus plotted on a logarithmic scale. The mean apparent Young's moduli given throughout the paper correspond to the geometric mean.

A trigger force of 0.45−0.55 nN was chosen for the measurements in this study. The z-range of the force curves was set to ≈1.3 μm. The velocities of the approach and retract curves were set to <850 μm/s, which ensured that the viscous drag forces on the cantilever remained below 0.1 nN (<20% of the trigger force). The resulting force curve rates were in a range of 150–350 Hz and allowed recording a force map with 128 × 128 pixels within 90−200 s.

D. Cell culture

Mouse embryonic wild-type fibroblasts (MEFs)[37] were cultured in low-glucose (1 g/l) Dulbecco's modified Eagle's medium (DMEM, Life Technologies, Carlsbad, CA, USA) supplemented with 10% (v/v) fetal calf serum (PAA Laboratories, Pasching Austria), 2 mM L-glutamine (PAA), and 100 U/ml penicillin–streptomycin (PAA) at 5% (v/v) CO_2 and 37 °C. Circular disks of muscovite mica with a diameter of 6 mm were attached to 0.1 mm thin plates of magnetic stainless steel with a diameter of 6 mm with a bio-compatible epoxy adhesive. This allowed fixing the samples magnetically to the stage. The mica surfaces were freshly cleaved and then functionalized by suspension in a 5 μg/ml solution of fibronectin (Roche Diagnostics, Mannheim, Germany) for ≈30 min at 37 °C. Subsequently the cells were seeded on the fibronectin coated mica surface. The living cells were imaged at 37 °C in CO_2-independent Leibovitz L-15 medium (Life Technologies, supplemented with 10% fetal calf serum) 24–48 h after seeding.

III. RESULTS AND DISCUSSION

A. Reducing viscous drag forces by using small cantilevers

To characterize the viscous drag forces, we recorded force curves with different force curve velocities on a freshly cleaved mica surface in distilled water. Both a conventional large contact mode cantilever and a small prototype cantilever were used. At a velocity of 250 μm/s the approach and retract parts for the large cantilever were significantly separated

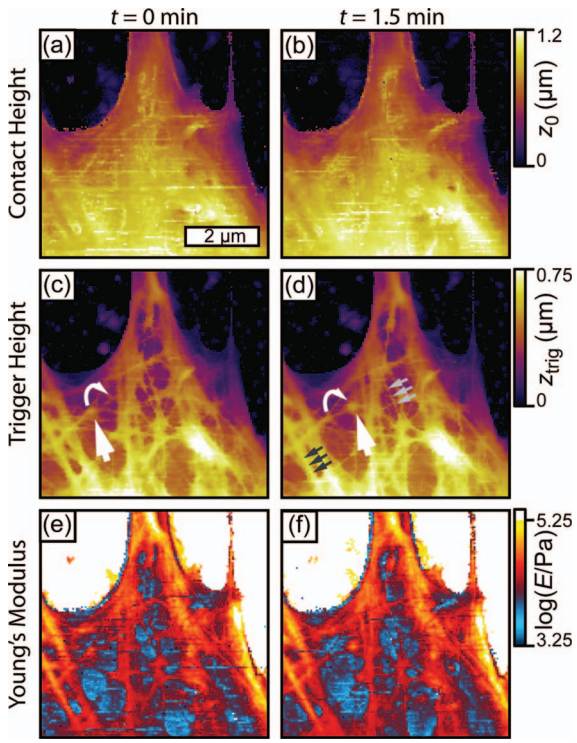

FIG. 2. Taking a look inside living cells by recording high resolution, high-speed force maps. (a) and (b) Contact height images, (c) and (d) trigger height images, and (e) and (f) apparent Young's modulus images from two consecutively recorded force maps on the periphery of a living MEF. While the contact height images show the fairly smooth surface of the plasma membrane, the trigger height and apparent Young's modulus images reveal the underlying network of cytoskeleton fibers. A small globular feature can be found in the trigger height images that changed its position in between the maps (white arrows in (c) and (d)). Force curve velocity 850 μm/s, force curve rate 333 Hz, 128 × 128 pixels.

from each other above the surface by a force $2F_{\text{visc}} = 2.1$ nN (Fig. 1(c), upper curve). In contrast, there was almost no separation observable for the small cantilever (Fig. 1(c), lower curve). A plot of the viscous drag force F_{visc} as a function of the force curve velocity shows a linear dependency for both cantilevers [Fig. 1(d)]. The proportionality factor ("viscous drag coefficient") was 44 times smaller for the small cantilever than for the large one ($0.098\frac{\mu\text{N}}{\text{m/s}}$, and $4.35\frac{\mu\text{N}}{\text{m/s}}$, respectively). This impressively demonstrates that small cantilevers are much less prone to viscous drag than large ones and consequently allow much faster force curve or force mapping measurements. Additionally, the smaller viscous drag coefficient of smaller cantilevers results in a smaller measured force noise in a given bandwidth.[24] This is apparent from the noise level in the non-contact region of both force curves [Fig. 1(c)], which was 4.1 times smaller for the small cantilever than for the large one (RMS value of 12.9 pN and 53.2 pN, respectively, in a bandwidth from 0.5 to 100 kHz). Small cantilevers are thus suited for both high-speed and low-noise force mapping measurements. The respective noise spectra of the thermal motion of the cantilevers in distilled water can be found in Fig. 2S in the supplementary material.[30]

A typical force curve recorded with a small cantilever and a velocity of 400 μm/s on a living MEF is shown in Fig. 1(e) (taken from frame 31 in Fig. 3). Sneddon's contact model was fitted to the approach part of the force curve (blacked dashed line), giving an apparent Young's modulus of 64 kPa. The cantilever was exposed to a viscous drag force of 35 pN, which is 13 times smaller than the preselected trigger force of 0.45 nN. At the same velocity the large cantilever from Fig. 1(c) would be exposed to a viscous drag force of 1.8 nN, which exceeds the trigger force by a factor of 4. Consequently, much larger trigger forces are required for large cantilevers, thereby inducing much larger and possibly destructive sample indentations. Note that the maximum imaging speed of the recently introduced force-curve-based imaging modes of Bruker (PeakForce tapping) and JPK (QI mode) is also limited by the viscous drag of the cantilever. These imaging modes would therefore also benefit significantly from the use of smaller cantilevers.

B. Taking a look inside living cells

Figure 2 shows two subsequent force maps (left and right column) that were recorded with high speed (350 Hz force curve rate) and at high resolution (128 × 128 pixels) on the periphery of a living MEF. The contact height images (a) and (b) show the substrate (black) and the relatively smooth surface of the cell body (violet-yellow). In contrast, the trigger height images (c) and (d) reveal a branched network of fibers with widths ranging from ≈60 nm (grey arrows) to ≈300 nm (black arrows). These fibers correspond to the cytoskeleton, which becomes visible when the tip indents the cell and probes structures lying beneath the surface.[12] The high aspect ratio of the small cantilever tip leads to small contact areas even for large sample indentations (between 200 and 600 nm) and thereby provides a high lateral resolution. A comparison of the trigger height images (c) and (d) shows that the structure of the fiber network remained almost unchanged within the acquisition time of 1.5 min. However, a globular feature with a width of ≈300 nm is visible that changed its position in between both images (straight and curved white arrow in (c) and (d)).

The local apparent Young's modulus E on the cell varies from 5 to 120 kPa [Figs. 2(e) and 2(f)]. Areas where the membrane was supported by underlying cytoskeleton fibers appear significantly stiffer (red, 25–120 kPa) than areas where the membrane was not supported (blue, 5–15 kPa). The geometric mean of the apparent Young's modulus of the cell body was $\bar{E} = 20$ kPa.

The force maps do not allow a precise identification of the observed cytoskeleton fiber type (microtubules, actin filaments, or intermediate filaments). It is known, however, that the cortical layer and the cell edges mainly consist of actin and actin-binding proteins such as myosin motors that regulate the tension of the cytoskeleton. Microtubules and intermediate filaments, on the other hand, are mainly present in the center of the cell.[38,39] Since the indentation was only 200–300 nm on top of the observed fibers, they presumably consist of actin.

C. Long-term, high-speed force mapping

The force map sequence shown in Fig. 3 was recorded within 108 min on the periphery of a living MEF (see video

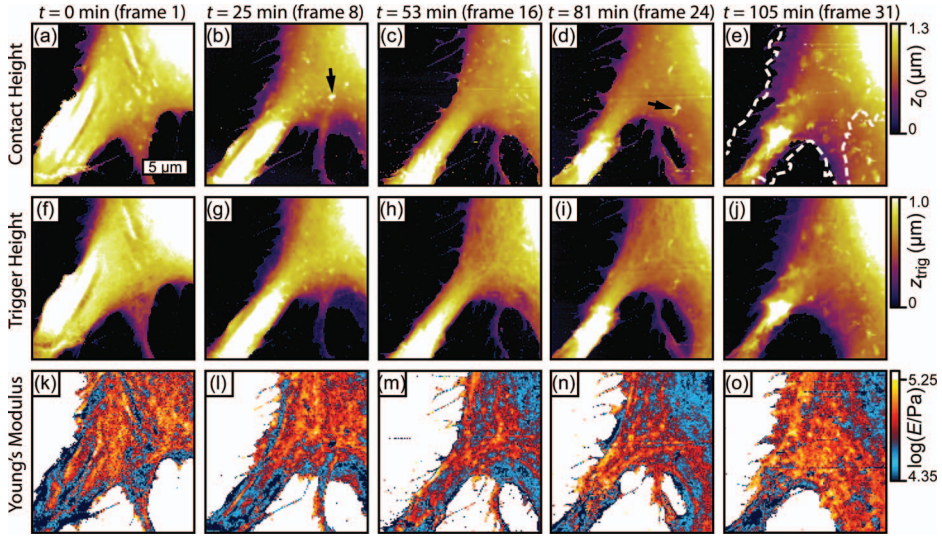

FIG. 3. Long-term, high-speed force mapping on the periphery of a living MEF. (a)–(e) Contact height images, (f)–(j) trigger height images, and (k)–(o) apparent Young's modulus images from a sequence of 31 force maps acquired over 108 min. The shape of the cell and its local apparent Young's modulus undergo significant changes, indicating a reorganization of the underlying cytoskeleton network. The white dashed line in (e) shows the contour of the cell at $t = 0$. Force curve velocity 400 μm/s, force curve rate 151 Hz, 128 × 128 pixels. (Multimedia view) [URL: http://dx.doi.org/10.1063/1.4885464.1]

for all 31 force maps). Significant changes in the cell's morphology and mechanics are apparent. A comparison between the cell's contour observed at $t = 0$ [white dashed line in Fig. 3(e)] and $t = 105$ min indicates the regions, where the cell had grown or retracted. The contact height images (a)–(e) show small microvilli-like structures with a width of ≈1 μm and a height of 100–500 nm on the cell surface that are highly dynamic (e.g., small black arrows in (b) and (d)). The apparent Young's modulus images (k)–(o) vary with time, suggesting structural changes in the cell's cytoskeleton. At $t = 0$ the geometric mean of the cell's apparent Young's modulus in the imaged area was relatively large ($\bar{E} \approx 67$ kPa), then decreased to ≈50 kPa at $t = 53$ min and finally increased again to ≈65kPa at $t = 105$ min. Individual cytoskeleton fibers are resolved less clearly in the trigger height images (f)–(j) (compared to Fig. 2) due to the large scan size of 18 μm × 18 μm.

The observed dynamics demonstrates that the induced tip-sample forces did not severely weaken or damage the cell. Also, we did not identify image artifacts in the force maps that could be explained by cellular debris attaching to and detaching from the tip over time (e.g., degradation of image contrast or sudden changes in height or Young's modulus). Consequently, high-speed force mapping is suited for long-term investigations of living cells.

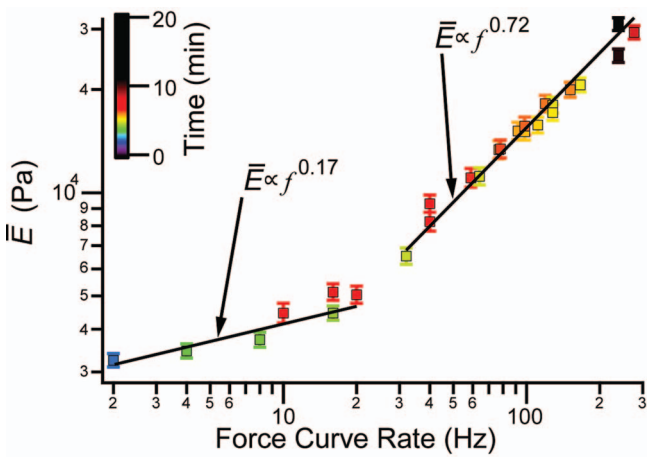

FIG. 4. Dependency of the apparent Young's modulus of a living MEF on the force curve rate. The data points correspond to the geometric mean of the apparent Young's modulus from force maps (15 × 15 pixels) recorded on top of the cell. The error bars show the geometric standard error. The modulus increased by a factor of 10 when increasing the force curve rate from 2 to 300 Hz. The force curve rate was changed randomly between the maps to make the measurement insensitive to a slow reorganization of the underlying cytoskeleton network (color of the data points corresponds to the time of acquisition of the map). All maps were recorded within 20 min. The contact height in the mapped area was 3.2 μm on average, which is significantly larger than the maximum indentation (≈600−300 nm). This allowed neglecting contributions from the underlying substrate on the measured modulus, because such contributions were found to be insignificant for indentations smaller than ≈25% of the cell's local height.[47] Figure 3S in the supplementary material[30] shows a high resolution contact height image of the investigated MEF and two trigger height images of the investigated scan area recorded immediately before and after the measurement series.

D. Velocity dependence of the apparent Young's modulus

In previous conventional force mapping studies (force curve rates ≈1 Hz), the average modulus of MEFs was found to be well below 10 kPa.[7,40] This is significantly less compared to the moduli found above. It has been shown that the measured apparent Young's modulus of eukaryotic cells increases with the force curve velocity owing to the viscoelastic nature of the cells.[39,41–43] The previous studies were conducted with force curve velocities below ≈60 μm/s, which is up to 14 times smaller than the force curve velocities used here. We thus investigated the dependence of the apparent Young's modulus on the force curve rate by recording force maps with 15 × 15 pixels and a rate in between 2 and 300 Hz in a small area on top of a MEF. The corresponding force curve velocities ranged from 5 to 800 μm/s (z-range of ≈1.3 μm). For a force

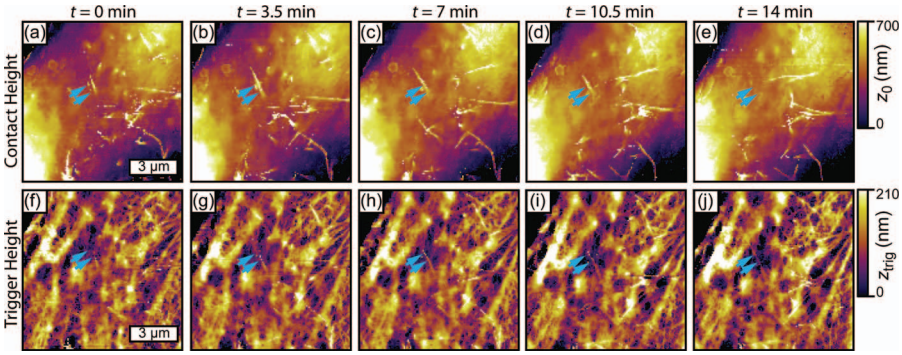

FIG. 5. Growing fibers observed by time-lapse force mapping. Data from five consecutive force maps are shown. (a)–(e) Contact height images. (f)–(j) Trigger height images (third order polynomial plane fit subtracted for better visibility). The growth process of a distinct fiber is indicated by small blue arrows. Force curve velocity 400 μm/s, force curve rate 158 Hz, 128 × 128 pixels. (Multimedia view) [URL: http://dx.doi.org/10.1063/1.4885464.2]

curve rate of 2 Hz an apparent Young's modulus of ≈3 kPa (Fig. 4) was measured, which is in accordance with previous studies.[7,40] As expected, the apparent Young's modulus increased when increasing the force curve rate. An apparent Young's modulus of ≈30 kPa was found for a force curve rate of 300 Hz.

Interestingly, the apparent Young's modulus increased with a significantly smaller slope for force curve rates f in a region between 2 and 20 Hz than for larger rates in a region between 20 and 300 Hz (on a double-logarithmic scale). Fitting the two data regions with a power law $\bar{E}(f) \alpha f^{\beta}$ gave an exponent β of 0.17 and 0.72, respectively. A similar power law behavior was found for the complex dynamic modulus of living cells by different types of microrheological measurements.[38,44–46] However, force curves induce non-sinusoidal stresses and strains. A direct comparison between the apparent Young's modulus and the complex dynamic modulus is thus difficult.

The observed stiffening of the cells at increasing frequencies offers a practical advantage in high-speed force mapping over conventional force mapping, since larger trigger forces can be used, which improves the signal to noise ratio of the measurement.

E. Observation of growing fibers

The force map sequence shown in Fig. 5 (see video) reveals several fiber-like structures growing on or near the surface of a living MEF. A distinct fiber is indicated by small blue arrows in the contact height images (a)–(e) and trigger height images (f)–(j). At $t = 0$ min, the length of the indicated fiber was measured as ≈1 μm in the contact height image (a) and ≈0.5 μm in the trigger height image (f). At $t = 7$ min the fiber length increased to ≈2 μm in the contact height image (c) and to ≈1.5 μm in the trigger height image (h). In the contact height images the fiber length subsequently decreased again to ≈1.5 μm at $t = 10.5$ min (d) and the fiber finally vanished at $t = 14$ min (e). In the trigger height images, however, the fiber remained visible with a length of ≈2 μm (j), which indicates that it has moved from the cell surface toward the underlying cytoskeleton. The whole sequence consists in complete of 14 force maps, which reveal more fibers with similar dynamics (see video). The growth rates of the fibers measured from the trigger height images vary between 2 and 10 nm/s. More growing fibers can be viewed in Fig. 6 (see video).

The observed dynamics likely reveals the polymerization of actin filaments or filament bundles, a process which is essential for the morphology, motility, and mechanics of eukaryotic cells.[48,49] The real-time polymerization of individual actin filaments has been observed on streptavidin 2D crystal substrates by high-speed tapping mode AFM.[50] To our knowledge such a growth process has not been imaged before by AFM inside a living eukaryotic cell.

F. Endocytosis

Figure 6 (see video) shows six contact height images obtained from a force map sequence recorded on top of a living MEF. Several small pits can be identified on the surface of the plasma membrane. The pits appeared and then disappeared ≈2–6 min later by forming protrusions (colored arrows). The protrusions had a height of 220 ± 25 nm (mean ± standard error of the mean, $n = 14$) and usually disappeared 2–4 min after pit closure.

The observed pits may be formed during endocytosis, a process in which cells absorb large molecules such as proteins

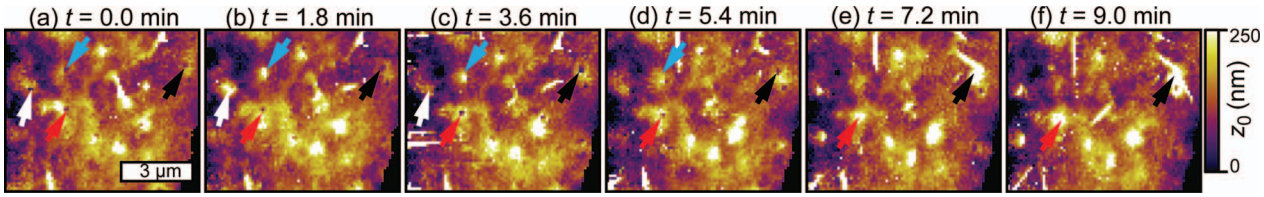

FIG. 6. Endocytosis. (a)–(f) Contact height images from a sequence of six consecutive force maps recorded on a living MEF. The sequence shows several endocytic pits in the cell membrane that close over time by forming a protrusion (arrows). The images are zoom-ins (60 × 80 pixels) to the recorded force maps. Force curve velocity 590 μm/s, force curve rate 227 Hz, 128 × 128 pixels. (Multimedia view) [URL: http://dx.doi.org/10.1063/1.4885464.3]

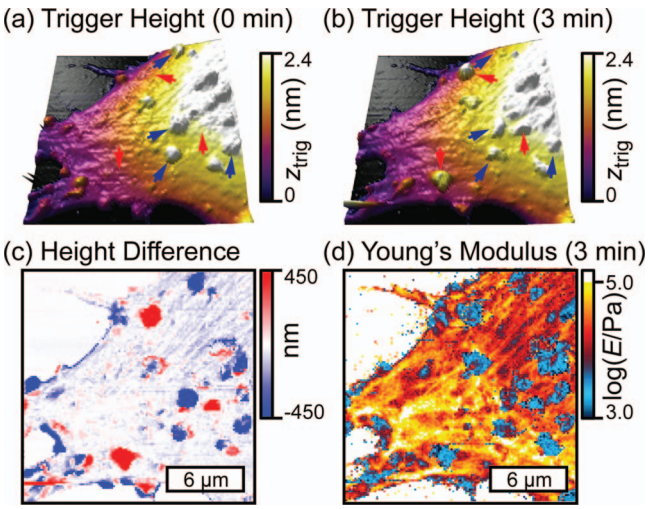

FIG. 7. Blebbing of a MEF. (a) and (b) 3D-rendered trigger height of two consecutive force maps. Several irregular bulges ("blebs") were found on the cell surface that grew or shrank with time (red and blue arrows, respectively). (c) Height difference, showing regions that increased (red) and decreased (blue) in height. (d) Apparent Young's modulus of the second force map. The blebs were, on average, about one order of magnitude softer than the surrounding cell body. Force curve velocity 600 μm/s, force curve rate 231 Hz, 128 × 128 pixels. (Multimedia view) [URL: http://dx.doi.org/10.1063/1.4885464.4]

that cannot pass through the plasma membrane. In course of endocytosis, small pits are formed in the membrane to enclose the molecules, thereby forming lipid vesicles, which are then transported into the cytoplasm.[51] Endocytic pits that closed by the formation of protrusions have already been observed by scanning ion conductance and fluorescence microscopy in the cell membrane of COS-7 and NIH-3T3 fibroblasts.[52,53] A similar process was imaged recently by high-speed tapping mode AFM on living HeLa cells.[27]

G. Blebbing

On some MEFs, several large irregular bulges with a width of ≈1–4 μm and a height of up to 2 μm were found, which either grew (red arrows) or shrank (blue arrows) with time [Figs. 5(a) and 7(b)]. The height difference between both images highlights the growing (red) and shrinking (blue) bulges [Fig. 7(c)]. The apparent Young's modulus of these bulges was significantly smaller (≈3.5 kPa) compared to the surrounding cell surface (≈30 kPa) [Fig. 7(d)]. A short video of the full force map sequence showing the apparent Young's modulus overlaid on the 3D-rendered trigger height topography can be found in the supplemental data (consisting of 6 force maps acquired within 14 min). The video shows that some bulges disappear entirely, both in the topography and in the apparent Young's modulus image.

The bulges presumably correspond to "blebs". Cell blebbing or zeiosis is a process that can occur during cell division, cell migration, apoptosis, or due to chemical and physical stress.[54,55] The three stages of zeiosis start with the localized decoupling of the plasma membrane from the cortical cytoskeleton or by a local rupture of the cell cortex. Subsequently, a membrane bulge grows due to the pressure inside the cell, which is believed to be caused by contractile actomyosin in the cell cortex.[56] In the final stage of blebbing the cortex gradually recovers, which leads to a retraction of the bleb. AFM has previously been applied to locally induce blebs in undifferentiated mouse embryonic stem cells by loading the cells locally with the AFM tip with large forces of 5–10 nN.[57] AFM contact mode imaging was also used to investigate the morphological changes of the cell due to blebbing in the course of apoptosis.[58] However, this seems to be the first demonstration that the AFM and in particular high-speed force mapping can reveal mechanical properties of a blebbing cell.

IV. CONCLUSIONS

We demonstrated the first high-speed AFM measurements in the force mapping mode allowing the measurement of local mechanical sample properties in addition to sample topography. For this purpose we adapted and improved our previously presented large-scan-range, high-speed AFM[23] to force mapping measurements on living eukaryotic cells. An enlarged z-range of 5.5 μm was used to overcome the large height differences found in the mouse embryonic fibroblasts investigated in this study. Displacement sensors were implemented to correct for the z-piezo nonlinearity in the recorded force curves and to enable closed loop scanning in xy with a maximum range of 19 μm×19 μm. A feedback-controlled micro-sample heater was implemented for long-term measurements at 37 °C. The viscous drag forces were reduced by a factor of 44 by employing small cantilevers. The combination of all these improvements allowed us to record force maps on living cells in liquids with force curve velocities of up to 850 μm/s, which is ≈10−100 times faster compared to conventional force mapping[4,5,8] and ≈4–10 times faster than the recently introduced force-curve-based imaging modes such as PeakForce tapping mode[19] or QI mode.[14,15] High-resolution force maps with 128×128 pixels were acquired within 1.5 min, thereby enabling the observation of several dynamic processes on living cells.

High-speed force map sequences were recorded on living cells for up to 2 h without inducing noticeable sample damage. About ten times higher apparent Young's moduli were measured by high-speed force mapping compared to conventional force mapping, which can be explained by the viscoelastic nature of cells. Our data revealed processes occurring on or closely beneath the plasma membrane such as endocytosis, cell blebbing, and the growth of individual fibers. The simultaneously obtained trigger height images provided detailed structural information from the underlying cytoskeleton. In conclusion, we showed that high-speed force mapping with small cantilevers is well suited for fast imaging of living cells, allowing to simultaneously record morphological and mechanical sample properties.

ACKNOWLEDGMENTS

We thank NanoWorld for providing the small cantilevers and for the scanning electron images of the small cantilever.

[1]M. Radmacher, J. P. Cleveland, M. Fritz, H. G. Hansma, and P. K. Hansma, Biophys. J. **66**(6), 2159–2165 (1994).
[2]M. Radmacher, M. Fritz, J. P. Cleveland, D. A. Walters, and P. K. Hansma, Langmuir **10**(10), 3809–3814 (1994).
[3]Y. Jiao and T. E. Schäffer, Langmuir **20**(23), 10038–10045 (2004).
[4]M. Radmacher, M. Fritz, C. M. Kacher, J. P. Cleveland, and P. K. Hansma, Biophys. J. **70**(1), 556–567 (1996).
[5]E. A-Hassan, W. F. Heinz, M. D. Antonik, N. P. D'Costa, S. Nageswaran, C. A. Schoenenberger, and J. H. Hoh, Biophys. J. **74**(3), 1564–1578 (1998).
[6]T. G. Kuznetsova, M. N. Starodubtseva, N. I. Yegorenkov, S. A. Chizhik, and R. I. Zhdanov, Micron **38**(8), 824–833 (2007).
[7]B. Fabry, A. H. Klemm, S. Kienle, T. E. Schäffer, and W. H. Goldmann, Biophys. J. **101**(9), 2131–2138 (2011).
[8]C. Rotsch and M. Radmacher, Biophys. J. **78**(1), 520–535 (2000).
[9]J. H. Hoh and A. Engel, Langmuir **9**(11), 3310–3312 (1993).
[10]O. Teschke, R. A. Douglas, and T. A. Prolla, Appl. Phys. Lett. **70**(15), 1977–1979 (1997).
[11]O. I. Vinogradova, H. J. Butt, G. E. Yakubov, and F. Feuillebois, Rev. Sci. Instrum. **72**(5), 2330–2339 (2001).
[12]U. G. Hofmann, C. Rotsch, W. J. Parak, and M. Radmacher, J. Struct. Biol. **119**(2), 84–91 (1997).
[13]P. Carl and H. Schillers, Pflug. Arch. Eur. J. Phys. **457**(2), 551–559 (2008).
[14]M. Horimizu, T. Kawase, T. Tanaka, K. Okuda, M. Nagata, D. M. Burns, and H. Yoshie, Micron **48**, 1–10 (2013).
[15]JPK Instruments AG, 2013, see http://www.jpk.com/afm.230.en.html.
[16]A. Rosa-Zeiser, E. Weilandt, S. Hild, and O. Marti, Meas. Sci. Technol. **8**(11), 1333–1338 (1997).
[17]J. Adamcik, A. Berquand, and R. Mezzenga, Appl. Phys. Lett. **98**(19), 193701 (2011).
[18]Y. F. Dufrêne, D. Martinez-Martin, I. Medalsy, D. Alsteens, and D. J. Müller, Nat. Methods **10**(9), 847–854 (2013).
[19]B. Pittenger, A. Slade, A. Berquand, P. Miliani, A. Boudaoud, and O. Hamant, Bruker, 2013, see www.bruker.com/nano.
[20]D. A. Walters, J. P. Cleveland, N. H. Thomson, P. K. Hansma, M. A. Wendman, G. Gurley, and V. Elings, Rev. Sci. Instrum. **67**(10), 3583–3590 (1996).
[21]T. Ando, N. Kodera, E. Takai, D. Maruyama, K. Saito, and A. Toda, Proc. Natl. Acad. Sci. U.S.A. **98**(22), 12468–12472 (2001).
[22]J. H. Kindt, G. E. Fantner, J. A. Cutroni, and P. K. Hansma, Ultramicroscopy **100**(3–4), 259–265 (2004).
[23]C. Braunsmann and T. E. Schäffer, Nanotechnology **21**(22), 225705 (2010).
[24]M. B. Viani, T. E. Schäffer, A. Chand, M. Rief, H. E. Gaub, and P. K. Hansma, J. Appl. Phys. **86**(4), 2258 (1999).
[25]Y. K. Yong, S. O. R. Moheimani, B. J. Kenton, and K. K. Leang, Rev. Sci. Instrum. **83**(12), 121101 (2012).
[26]Y. Suzuki, N. Sakai, A. Yoshida, Y. Uekusa, A. Yagi, Y. Imaoka, S. Ito, K. Karaki, and K. Takeyasu, Sci. Rep. **3**, 2131 (2013).
[27]H. Watanabe, T. Uchihashi, T. Kobashi, M. Shibata, J. Nishiyama, R. Yasuda, and T. Ando, Rev. Sci. Instrum. **84**(5), 053702 (2013).
[28]A. Colom, I. Casuso, F. Rico, and S. Scheuring, Nat. Commun. **4**, 2155 (2013).
[29]M. Jaschke and H. J. Butt, Rev. Sci. Instrum. **66**(2), 1258–1259 (1995).
[30]See supplementary material at http://dx.doi.org/10.1063/1.4885464 for Figs. 1S, 2S, and 3S.
[31]J. L. Hutter and J. Bechhoefer, Rev. Sci. Instrum. **64**(7), 1868–1873 (1993).
[32]T. E. Schäffer, Nanotechnology **16**(6), 664–670 (2005).
[33]S. Cook, T. E. Schäffer, K. M. Chynoweth, M. Wigton, R. W. Simmonds, and K. M. Lang, Nanotechnology **17**(9), 2135–2145 (2006).
[34]M. J. Higgins, R. Proksch, J. E. Sader, M. Polcik, S. Mc Endoo, J. P. Cleveland, and S. P. Jarvis, Rev. Sci. Instrum. **77**(1), 013701 (2006).
[35]I. N. Sneddon, Int. J. Eng. Sci. **3**(1), 47–57 (1965).
[36]C. Braunsmann, V. Prucker, and T. E. Schäffer, Appl. Phys. Lett. **104**(10), 103101 (2014).
[37]C. T. Mierke, P. Kollmannsberger, D. P. Zitterbart, G. Diez, T. M. Koch, S. Marg, W. H. Ziegler, W. H. Goldmann, and B. Fabry, J. Biol. Chem. **285**(17), 13121–13130 (2010).
[38]B. D. Hoffman and J. C. Crocker, Annu. Rev. Biomed. Eng. **11**, 259–288 (2009).
[39]S. Nawaz, P. Sanchez, K. Bodensiek, S. Li,M. Simons, and I. A. T. Schaap, PLoS One **7**(9), e45297 (2012).
[40]A. H. Klemm, S. Kienle, J. Rheinlaender, T. E. Schäffer, and W. H. Goldmann, Biochem. Biophys. Res. Commun. **393**(4), 694–697 (2010).
[41]M. H. Zhao, C. Srinivasan, D. J. Burgess, and B. D. Huey, J. Mater. Res. **21**(8), 1906–1912 (2006).
[42]M. J. Rosenbluth, W. A. Lam, and D. A. Fletcher, Biophys. J. **90**(8), 2994–3003 (2006).
[43]Z. L. Zhou, A. H. W. Ngan, B. Tang, and A. X. Wang, J. Mech. Behav. Biomed. **8**, 134–142 (2012).
[44]B. Fabry, G. N. Maksym, J. P. Butler, M. Glogauer, D. Navajas, and J. J. Fredberg, Phys. Rev. Lett. **87**(14), 148102 (2001).
[45]J. Alcaraz, L. Buscemi, M. Grabulosa, X. Trepat, B. Fabry, R. Farré, and D. Navajas, Biophys. J. **84**(3), 2071–2079 (2003).
[46]M. Balland, A. Richert, and F. Gallet, Eur. Biophys. J. **34**(3), 255–261 (2005).
[47]R. E. Mahaffy, C. K. Shih, F. C. MacKintosh, and J. Käs, Phys. Rev. Lett. **85**(4), 880–883 (2000).
[48]D. A. Fletcher and D. Mullins, Nature (London) **463**(7280), 485–492 (2010).
[49]A. Mogilner and K. Keren, Curr. Biol. **19**(17), R762–R771 (2009).
[50]D. Yamamoto, N. Nagura, S. Omote, M. Taniguchi, and T. Ando, Biophys. J. **97**(8), 2358–2367 (2009).
[51]G. Sahay, D. Y. Alakhova, and A. V. Kabanov, J. Controlled Release **145**(3), 182–195 (2010).
[52]A. I. Shevchuk, P. Hobson, M. J. Lab, D. Klenerman, N. Krauzewicz, and Y. E. Korchev, Pflugers Arch. **456**(1), 227–235 (2008).
[53]A. I. Shevchuk, P. Novak, M. Taylor, I. A. Diakonov, A. Ziyadeh-Isleem, M. Bitoun, P. Guicheney, M. J. Lab, J. Gorelik, C. J. Merrifield, D. Klenerman, and Y. E. Korchev, J. Cell Biol. **197**(4), 499–508 (2012).
[54]G. Charras and E. Paluch, Nat. Rev. Mol. Cell Biol. **9**(9), 730–736 (2008).
[55]G. T. Charras, C. K. Hu, M. Coughlin, and T. J. Mitchison, J. Cell Biol. **175**(3), 477–490 (2006).
[56]J. Y. Tinevez, U. Schulze, G. Salbreux, J. Roensch, J. F. Joanny, and E. Paluch, Proc. Natl. Acad. Sci. U.S.A. **106**(44), 18581–18586 (2009).
[57]A. L. Hemsley, D. Hernandez, C. Mason, A. E. Pelling, and F. S. Veratich, Cell Health Cytoskeleton **3**, 23–34 (2011).
[58]Y. G. Kuznetsov, A. J. Malkin, and A. McPherson, J. Struct. Biol. **120**(2), 180–191 (1997).